



TOWARDS THE VERIFICATION AND VALIDATION OF A 3-D EXPLICIT FINITE-DIFFERENCE ALGORITHM FOR AEROSPACE APPLICATIONS

Enda Dimitri Vieira Bigarelli

Centro Técnico Aeroespacial, Instituto Tecnológico de Aeronáutica
CTA/ITA/IEA - 12228-900 - São José dos Campos, SP, Brasil

João Luiz F. Azevedo

Centro Técnico Aeroespacial, Instituto de Aeronáutica e Espaço
CTA/IAE/ASE-N - 12228-904 - São José dos Campos, SP, Brasil

Abstract. *This work presents a description of a simple and easy-to-implement verification and preliminary validation method of numerical simulation tools. This method is applied to a 3-D aerodynamic solver developed at IAE for aerospace applications, such as satellite launchers and sounding rockets. This code is a 3-D, 2nd-order, finite difference algorithm written for a general, body conforming, curvilinear coordinate system and it solves the Euler equations. This reliable testing method consists in adopting known functions as solution for the primitive variables in a computational domain and introducing the right hand side operator for this known solution as a source term for the numerical equations. The code converges to a numerical solution which is then compared to the theoretical one. Average numerical errors obtained are of the order of 10^{-4} . Grid refinement studies are also performed for this computational domain. This effort includes the analysis of the algorithm sensitiveness with a refined grid direction as well as the influence of the grid spacing in the convergence of the method. Numerical results obtained for the Brazilian Satellite Launcher (VLS) are compared to available experimental data. This comparison shows that an average error of 5 to 10% is found between experimental and numerical results, which can be acceptable within engineering margins of error.*

Keywords. *CFD, Three-dimensional simulation, Aerospace application, Algorithm verification.*

1. INTRODUCTION

During the design process of an aerospace vehicle, one is required to determine the aerodynamics of these vehicles at angle of attack because this will provide loads required for the structural design of the vehicle as well as the flight dynamics stability characteristics necessary for the control system design. Azevedo, Zdravistch and Silva (1991) have performed axisymmetric viscous simulations for flows over the VLS with very good representation of the flow physics. Moreover, three-dimensional inviscid computations over the VLS at low angles of attack with good agreement with experimental data were also performed by Azevedo *et al.* (1996).

This earlier work, however, considered fairly simple 3-D geometries and, typically, mesh refinement was less than adequate due to computational resource limitations. This discussion emphasizes that the problem of simulating transonic and supersonic flows over complex vehicles is not a new requirement at IAE. However, recently, the development of the computational tools available in the CFD group, together with additional computational resources available in the country, have made possible the analysis of realistic configurations. Moreover, the computational grids can be made fine enough that real aerodynamic phenomena could be accurately represented and a physical analysis of these phenomena performed.

In this context, Basso, Antunes and Azevedo (2000) have presented results for the complete, 1st-stage flight, VLS configuration, which means that the multiblock capability of the solver has been exercised. The comparisons included in this work considered solely flight conditions at zero angle of attack. Results at other flight regimes, including flows at angle of attack, for single block configurations were presented by Bigarelli and Azevedo (1999) and Bigarelli, Mello and Azevedo (1999). This numerical code is a 3-D finite-difference code written for general, body-conforming, curvilinear coordinate systems and solves the Euler equations.

Since the development of this computational tool is aimed at actual design utilisation, it is very important that it is completely validated for the applications of interest. It is also necessary to address the dependency of the numerical code with respect to the computational grids, assessing the accuracy of the numerical solution with grid refinement and the sensitivity of the convergence rate with stretched directions of the mesh. A fast and accurate method of performing this preliminary verification is presented in this work. A source term carrying information of a preliminarily known solution of the equation system is explicitly added to the numerical formulation in order to drive the numerical solution to the known one. The difference between the converged computational solution and the original one can be a measure of the accuracy of the method as well as a confirmation of the correctness of the implementation. The forthcoming sections present the theoretical and the numerical formulation of the solver. The verification procedure is, then, described and the solver characteristics are assessed. A comparison between numericals result and experimental data for a typical aerospace configuration is finally performed.

2. THEORETICAL FORMULATION

The numerical code used solves the 3-D, compressible, Euler equations. These equations can be written in strong conservation-law form for general, body-conforming, curvilinear coordinates (Pulliam and Steger, 1980) as

$$\frac{\partial \bar{Q}}{\partial \tau} + \frac{\partial \bar{E}}{\partial \xi} + \frac{\partial \bar{F}}{\partial \eta} + \frac{\partial \bar{G}}{\partial \zeta} = J^{-1} S, \quad (1)$$

where the vector of conserved quantities, \bar{Q} , is defined as

$$\bar{Q} = J^{-1} \left[\rho \quad \rho u \quad \rho v \quad \rho w \quad e \right]^T, \quad (2)$$

and the inviscid flux vectors, \bar{E} , \bar{F} and \bar{G} , can be written as

$$\bar{E} = J^{-1} \left\{ \begin{array}{c} \rho U \\ \rho u U + p \xi_x \\ \rho v U + p \xi_y \\ \rho w U + p \xi_z \\ (e + p)U - p \xi_t \end{array} \right\}, \quad (3)$$

$$\bar{F} = J^{-1} \begin{pmatrix} \rho V \\ \rho u V + p \eta_x \\ \rho v V + p \eta_y \\ \rho w V + p \eta_z \\ (e + p)V - p \eta_t \end{pmatrix}, \quad (4)$$

$$\bar{G} = J^{-1} \begin{pmatrix} \rho W \\ \rho u W + p \zeta_x \\ \rho v W + p \zeta_y \\ \rho w W + p \zeta_z \\ (e + p)W - p \zeta_t \end{pmatrix}. \quad (5)$$

The vector S is the source term, which will be used to verify the accuracy of the implementation and the numerical code. It is given by the forthcoming general components

$$S = [s_1 \ s_2 \ s_3 \ s_4 \ s_5]^T. \quad (6)$$

In the usual CFD nomenclature, adopted in the present work, ρ is the density, u , v and w are the Cartesian velocity components, p is the pressure and e is the total energy per unity of volume. The pressure is obtained from the equation of state for perfect gases, written as

$$p = (\gamma - 1) \left[e - \frac{1}{2} \rho (u^2 + v^2 + w^2) \right], \quad (7)$$

where γ is the ratio of specific heats. The contravariant velocity components, U , V and W , were defined as

$$\begin{aligned} U &= \xi_t + \xi_x u + \xi_y v + \xi_z w, \\ V &= \eta_t + \eta_x u + \eta_y v + \eta_z w, \\ W &= \zeta_t + \zeta_x u + \zeta_y v + \zeta_z w. \end{aligned} \quad (8)$$

Expressions for the Jacobian of the transformation, J , and for the various metric terms can be found in Pulliam and Steger (1980).

3. NUMERICAL IMPLEMENTATION

The governing equations are discretised in a finite difference context. The spatial discretisation adopted uses a 2nd-order, central difference algorithm plus explicitly added artificial dissipation terms in order to control nonlinear instabilities. The equations, fully discretised in space, can be written as

$$\left(\frac{\partial \bar{Q}}{\partial \tau} \right)_{i,j,k} = -\text{RHS}_{i,j,k}. \quad (9)$$

The right-hand side operator of Eq. (9) is defined as

$$\begin{aligned} \text{RHS}_{i,j,k} &= \frac{1}{2 \Delta \xi} (\bar{E}_{i+1,j,k} - \bar{E}_{i-1,j,k}) + \frac{1}{2 \Delta \eta} (\bar{F}_{i,j+1,k} - \bar{F}_{i,j-1,k}) \\ &+ \frac{1}{2 \Delta \zeta} (\bar{G}_{i,j,k+1} - \bar{G}_{i,j,k-1}) \\ &- \frac{1}{\Delta \xi} (J_{i+1/2,j,k}^{-1} d_{i+1/2,j,k} - J_{i-1/2,j,k}^{-1} d_{i-1/2,j,k}) \\ &- \frac{1}{\Delta \eta} (J_{i,j+1/2,k}^{-1} d_{i,j+1/2,k} - J_{i,j-1/2,k}^{-1} d_{i,j-1/2,k}) \\ &- \frac{1}{\Delta \zeta} (J_{i,j,k+1/2}^{-1} d_{i,j,k+1/2} - J_{i,j,k-1/2}^{-1} d_{i,j,k-1/2}) \\ &- J_{i,j,k}^{-1} S_{i,j,k}, \end{aligned} \quad (10)$$

where $\Delta\xi = \Delta\eta = \Delta\zeta = 1$ for the general curvilinear coordinate case. An anisotropic scalar artificial dissipation method, as described in Turkel and Vatsa (1994), was used. This scheme is nonlinear and allows a selection between artificial dissipation terms of second and fourth differences, which is very important in capturing shock waves in the flows of interest of aerospace engineering.

Time march uses an explicit, second order, five-stage Runge-Kutta scheme, as seen in Jameson, Schmidt and Turkel (1981) and Jameson and Mavriplis (1986), which can be written as

$$\begin{aligned}\overline{Q}_{i,j,k}^{(0)} &= \overline{Q}_{i,j,k}^n, \\ \overline{Q}_{i,j,k}^{(\ell)} &= \overline{Q}_{i,j,k}^{(0)} - \alpha_\ell \Delta t_{i,j,k} \text{RHS}_{i,j,k}^{(\ell-1)}, \quad \ell = 1, 2, \dots, 5, \\ \overline{Q}_{i,j,k}^{n+1} &= \overline{Q}_{i,j,k}^{(5)}.\end{aligned}\tag{11}$$

Numerical values for the α_ℓ parameters can be found in Jameson and Mavriplis (1986). In the previous expressions, Δt stands for the time step, and n and $n + 1$ refer to the property values at the start and at the end of each time step. Equation (11) also indicates that a local time step option is being used in order to accelerate convergence to steady state calculations.

4. VERIFICATION PROCEDURE

For the steady-state solution of the Euler equations, the time-derivative of the vector of conserved properties is obviously zero. Thus, Eq. 1 can be rewritten at the steady-state condition as

$$\frac{\partial \overline{E}}{\partial \xi} + \frac{\partial \overline{F}}{\partial \eta} + \frac{\partial \overline{G}}{\partial \zeta} = J^{-1}S.\tag{12}$$

If there exists a solution of the conserved variables, or one is provided by the user, the convective fluxes \overline{E} , \overline{F} and \overline{G} can be easily calculated by hand. Hence, the source term S can also be determined from the steady-state condition presented in Eq. 12. Adding this source term to the right-hand side operator of the numerical code, as presented in Eq. 10, a correctly implemented computational method should drive the computational solution to the originally provided one. The difference between the computational solution, driven by this source term explicitly added to the method, and the provided solution can be used as a measure of the correctness of the implementation.

For this work, known functions were chosen for the primitive variables of the formulation, given by the static pressure p , velocity components in three-dimensions u , v and w , and the density ρ . The solution for these variables was defined as

$$\begin{pmatrix} \rho \\ u \\ v \\ w \\ p \end{pmatrix} = \begin{pmatrix} \tanh(x + y + z) \\ \tanh^3(x + y + z) \end{pmatrix},\tag{13}$$

where x , y and z are the nondimensionalized Cartesian components of the physical domain. It is interesting to state that the solution was provided for the primitive variables, instead of the conserved variables, which would be the straightforward option at a first sight, for the forthcoming reasons:

- It is necessary to avoid unphysical balance of the provided solution, such as negative pressure.

- The primitive variables are the ones which really carry a physical meaning for engineering applications.
- It would be a more demanding test case for the method to receive a forcing term for the primitive variables but solve for the conserved ones.

If one substitutes the primitive variables given in Eq. 13 at Eq. 12 and performs some simple algebra, the source term components can be written as

$$S_{i,j,k} = \left\{ \begin{array}{l} 6 \frac{\tanh(x+y+z)}{\cosh^2(x+y+z)} \\ 12 \frac{\tanh^2(x+y+z)}{\cosh^2(x+y+z)} \\ 12 \frac{\tanh^2(x+y+z)}{\cosh^2(x+y+z)} \\ 12 \frac{\tanh^2(x+y+z)}{\cosh^2(x+y+z)} \\ \left(\frac{30\gamma-18}{\gamma-1} \right) \frac{\tanh^3(x+y+z)}{\cosh^2(x+y+z)} \end{array} \right\}_{i,j,k} \quad (14)$$

The numerical method is, then, evaluated by a comparison of the simulation results with the provided solution, given in Eq. 13. This comparison was made using the maximum value and the L_2 norm of the difference between both solutions in the field.

5. BOUNDARY CONDITIONS AND COMPUTATIONAL GRIDS

The physical domain chosen for the verification procedure was a quadrilateral block with unitary sides. Various grid configurations were used for the simulations, including different number of grid points at the three directions as well as stretching in one direction. With these different computational meshes, the authors would like to address the behaviour of the numerical code with different grid characteristics. The interest was mostly directed towards the effect of the highly stretched distribution on the convergence of the method, since it is known in the literature that explicit methods are very sensitive to that, and towards any degradation of the numerical solution with increasing grid spacing.

For an aerospace configuration, which is the application of interest of the group, the types of boundary conditions that should be considered include solid walls, far field boundaries, symmetry, upstream centerline and downstream (exit) conditions. For the rocket wall, the velocity vector is set tangent to the wall, and a zero-order extrapolation of the pressure and the density is performed. The upstream centerline is a singularity of the coordinate transformation and, in the present case, the approach consists in extrapolating the property values from the adjacent longitudinal plane and in averaging the extrapolated values in the azimuthal direction in order to define the updated properties. At the exit plane, the boundary conditions are implemented through the use of the 1-D characteristic relations for the 3-D Euler equations. Freestream properties are assumed at the far field boundaries. Furthermore, in order to reduce computational costs, computational grids used are generated for half a body in the azimuthal direction. Hence, symmetry is applied in the pitching plane using two auxiliary extra planes added, respectively, before the leeside and after the windside pitching plane. For the verification procedure, these boundary conditions unfortunately could not be tested. In order to keep coherence with the source terms added, boundary conditions of the Dirichlet type should be used, which means that the values of the conserved properties must be provided at the boundaries for the verification tests.

5. RESULTS

In this section, the results obtained with the already discussed verification method are presented. Two important characteristics of the solver, which mostly depend on the mesh

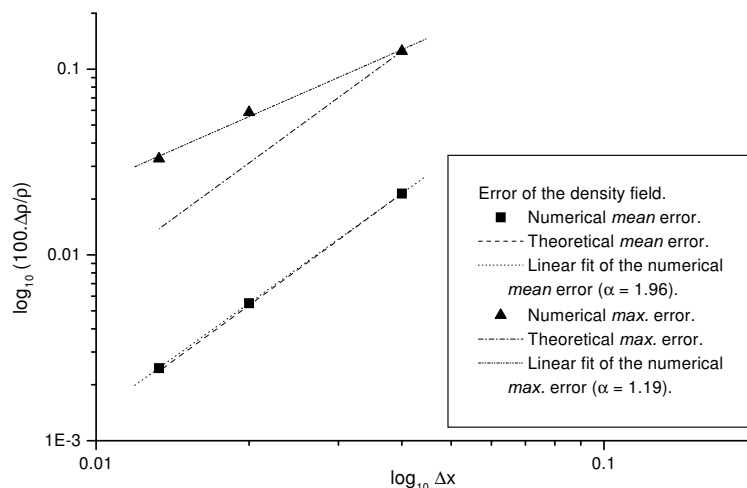


Figure 1: Mean and maximum percentual errors for the numerical density field.

topology, are stressed here. These are the convergence speed of the code and the accuracy of the spatial derivatives. In this work, a 2nd-order approximation of spatial derivatives were used. Hence, the numerical error of the method can be written as

$$\text{error} \propto \Delta x^2, \quad (15)$$

where Δx is the smallest grid spacing. If one applies a logarithmic function at both sides of Eq. 15, this equation can be rewritten as

$$\log_{10}(\text{error}) \propto 2 \log_{10}(\Delta x). \quad (16)$$

The logarithmic of the theoretical error of the method has a slope of two when plotted against the logarithmic of the smallest grid spacing. However, the actual spatial accuracy of the method may be different from that presented in Eq. 16. It is written for a general case as

$$\log_{10}(\text{error}) \propto \alpha \log_{10}(\Delta x), \quad (17)$$

where α is the slope of the actual spatial accuracy that can be attained with the method implemented. The comparison between the slope coefficients of Eqs. 16 and 17 will be used to assess the actual spatial accuracy of the solver.

Figure 1 presents the maximum and the mean percentual error of a directly solved variable against the grid spacing. For these results, three meshes with constant grid spacing and $25 \times 25 \times 25$, $50 \times 50 \times 50$ and $75 \times 75 \times 75$ points, respectively, were used. The variable chosen is the nondimensionalized density. It can be clearly seen in this figure that the mean error curve follows almost exactly the theoretical one, with $\alpha = 1.96$. This fact means that the numerical code really solves the conserved properties with second order of accuracy. It can also be observed that the mean error level is very low, about 0.01%, which represents a remarkably correctness of the numerical method. If one consider now the maximum error, one verifies that it presents an almost first-order spatial accuracy behaviour, with $\alpha = 1.19$. This maximum error is precisely located at the boundaries of the field, where the fourth derivatives of the artificial dissipation model are neglected in order to decrease the size of the calculation stencil. Only second derivatives, which are associated with terms of first-order spatial accuracy for the artificial dissipation model currently used, are considered. This clearly affects the local spatial accuracy, but not the overall accuracy of the method. Hence, it corroborates the idea of trading off local spatial accuracy for a simpler implementation and lower computational costs.

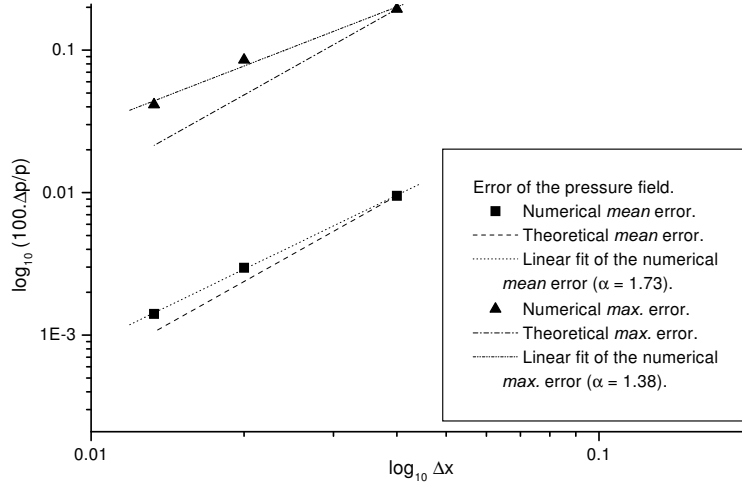


Figure 2: Mean and maximum percentual errors for the numerical pressure field.

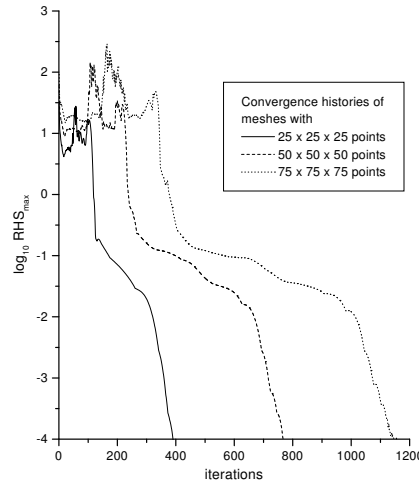


Figure 3: Residue histories for three meshes with constant grid spacing.

Similar results for the maximum and the mean percentual errors for an indirectly solved variable are presented in Fig. 2. The same meshes considered in the results of Fig. 1 were used and the variable analysed is the nondimensionalized pressure. Spatial accuracy for the mean error is lower than expected, with $\alpha = 1.73$. However, the average value is very low, attaining the same order of that found in the density results. Spatial accuracy for the maximum error is a bit higher in this case, with $\alpha = 1.38$.

It is known in the literature that the convergence of explicit methods have a large sensitivity with highly stretched grids, due to the increase in the measure of the stiffness of the problem. It is also known that refined grids are more difficult to solve, resulting in very low convergence rates. Figure 3 presents some results that corroborate this statement. Residue histories for the same meshes considered in Figs. 1 and 2, that is, with constant grid spacing, are shown in this figure. One can clearly see that, the more refined the grid, the slower the convergence rate. This behaviour can get worse if one now considers meshes with one highly-stretched direction. Fig. 4 presents the residue histories for meshes with the same number of points of the grids of Fig. 3 but with direction η stretched with an exponential growth of 11%. It is observed in this figure that the convergence rate gets very poor for more refined grids. As stated before, this behaviour was expected. However, in the applications of interest, meshes are usually very refined and stretched in the normal direction to the wall in

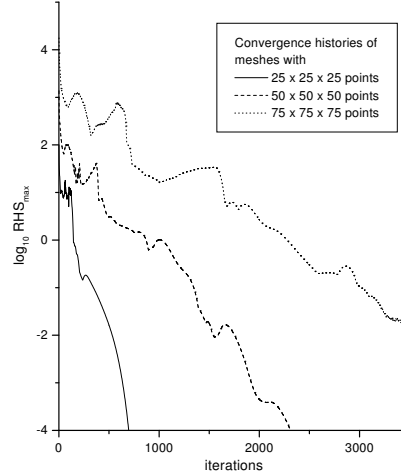


Figure 4: Residue histories for three meshes with one grid direction stretched with an exponential growth of 11%.

order to capture boundary layer phenomena. Thus, aiming at accelerating the convergence, the group is currently working at implementing a multigrid scheme and seriously considering the application of an implicit time march procedure, which better handles grids with such topology.

Finally, a comparison between computational results and available experimental data for the Brazilian Satellite Launcher (VLS) can be seen in Fig. 5. Flight conditions considered are $M_\infty = 3.00$ and $\alpha = 4$ deg. Numerical simulations used a thin-layer approximation to the compressible Navier-Stokes equations, with $Re = 30$ million, based on the vehicle after-body diameter. This figure presents pressure coefficient, C_p , distributions along the vehicle wall. These results indicate that the experimental data and the computational solution do not present large differences. In particular, the correct trends in the C_p distribution are captured by the numerical simulation. Mach number contours for the same flight condition can be found in Fig. 6. Several other similar comparisons, at different flight conditions, are available for flow simulations over the VLS. However, the comparison shown in the figures presented above is representative of the level of agreement which can be obtained between the experimental data and the computational simulation results throughout the speed range of interest.

6. CONCLUDING REMARKS

This work presents a capability implemented at IAE to solve three-dimensional flows over complex aerospace configurations at angle of attack to determine important aerodynamic loads required at the design stage. A computational code which solves the 3-D Euler equations for general, body-conforming, curvilinear coordinates was developed. The validation and the assessment of the characteristics of the numerical code are essential steps towards a reliable and robust application of the solver for the objectives of interest. Thus, a simple and reliable method for verifying the correctness of the numerical code was used.

Some validation analyses involved comparison of computational results and theoretical data, in terms of mean and maximum error between numerical and theoretical solutions. It was observed that mean errors are of the order of 0.01% for very coarse grids and even lower for more refined ones. It could also be seen that the convergence rate is affected by grid stretching and refinement. Finally, numerical results obtained for a typical aerospace configuration were compared to experimental data. Good agreement was observed, which is representative of the level of agreement which can be obtained between the experimental data and the computational simulation results.

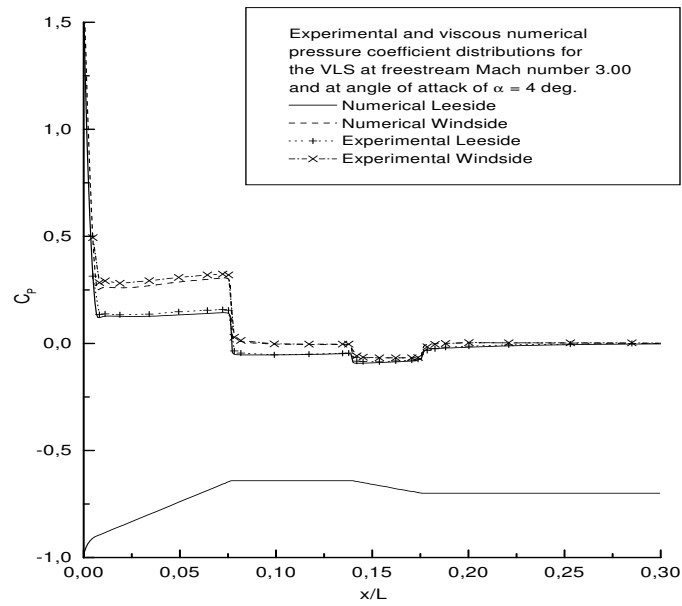


Figure 5: Numerical C_p distributions compared to experimental data for the VLS central body at $\alpha = 4$ deg. and $M_\infty = 3.00$. Reynolds number is 30 million.

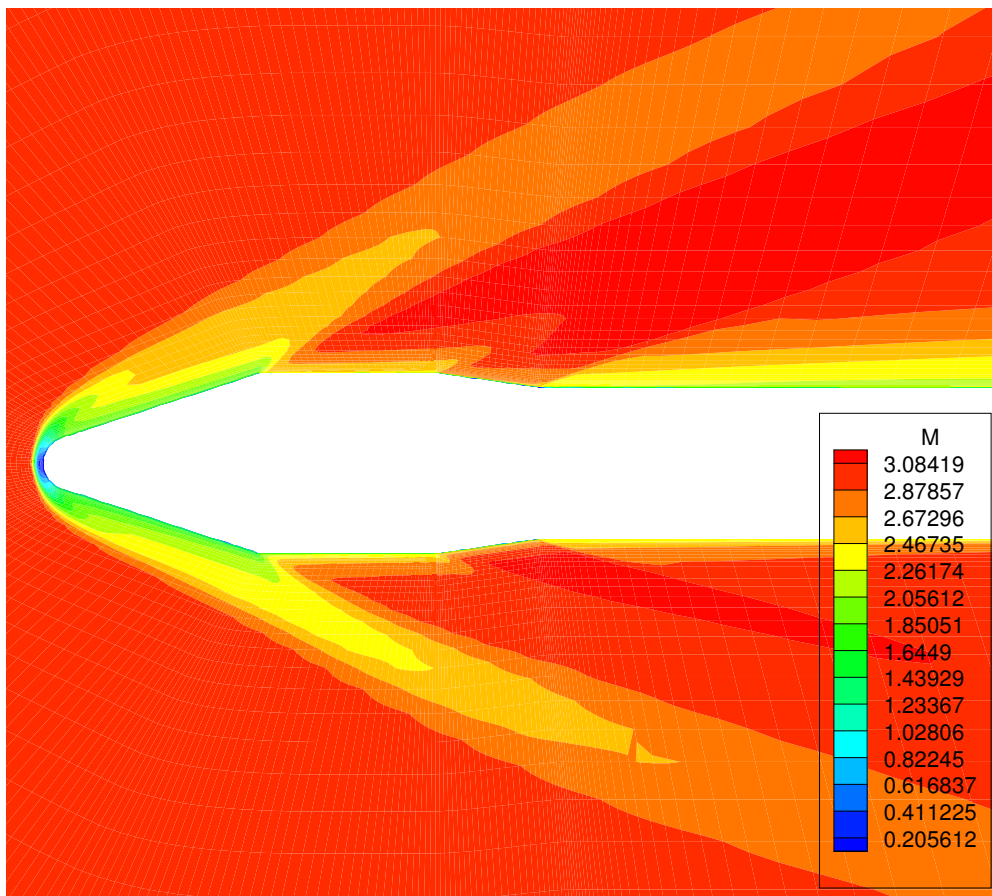


Figure 6: Mach number contours for the VLS central body at $\alpha = 4$ deg. and $M_\infty = 3.00$. Reynolds number is 30 million.

One should observe that several other vehicles are currently being developed, or improved, within the range of responsibilities of IAE. Due to budgetary constraint in the country, it is not always possible to take these other vehicles to the wind tunnel, especially because this typically means performing tests overseas. The approach which is currently being pursued is to use the experimental data available for the VLS to validate the present computational tools under development. Hence, this flow simulation capability can be applied to the other vehicles of interest, since the overall configurations are not that different from the VLS central body.

7. ACKNOWLEDGEMENTS

The first author has received support from Fundação de Amparo à Pesquisa do Estado de São Paulo, FAPESP, under the graduate scholarship of Project No. 00/13.652-6. Additional support received from Conselho Nacional de Desenvolvimento Científico e Tecnológico, CNPq, under the Integrated Project Research Grant No. 522.413/ 96-0, is also acknowledged.

8. REFERENCES

- Azevedo, J.L.F., Moraes, P., Jr., Maliska, C.R., Marchi, C.H. and Silva, A.F.C., 1996, "Code Validation for High-Speed Flow Simulation over Satellite Launch Vehicle," *Journal of Spacecraft and Rockets*, Vol. 33, No. 1, pp. 15-21.
- Azevedo, J.L.F., Zdravistch, F. and Silva, A.F.C., 1991, "Implementation and Validation of Euler Solvers for Launch Vehicle Flows," *Proceedings of the Fourth International Symposium on Computational Fluid Dynamics*, Vol I, Davis, CA, USA, pp. 42-47.
- Basso, E., Antunes, A.P., Azevedo, J.L.F., 2000, "Three Dimensional Flow Simulations Over a Complete Satellite Launcher with a Cluster Configuration," *Proceedings of the 18th AIAA Applied Aerodynamics Conference and Exhibit*, Denver, CO, USA, pp. 805-813.
- Bigarelli, E.D.V. and Azevedo, J.L.F., 1999, "Calculation of the Aerodynamic Loads over the Sonda III-A Vehicle on Transonic and Supersonic Flow Conditions," Report No. 524-000000/B1001, Instituto de Aeronáutica e Espaço, São José dos Campos, SP, Brazil (in Portuguese).
- Bigarelli, E.D.V., Mello, O.A.F. and Azevedo, J.L.F., 1999, "Three Dimensional Flow Simulations for Typical Launch Vehicles at Angle of Attack," *Proceedings of the 15th Brazilian Congress of Mechanical Engineering – COBEM 99*, Águas de Lindóia, SP, Brazil (publication in CD-ROM without page numbering).
- Jameson, A. and Mavriplis, D., 1986, "Finite Volume Solution of the Two-Dimensional Euler Equations on a Regular Triangular Mesh," *AIAA Journal*, Vol. 24, No. 4, pp. 611-618.
- Jameson, A., Schmidt, W. and Turkel, E., 1981, "Numerical Solution of the Euler Equations by Finite Volume Methods Using Runge-Kutta Time-Stepping Schemes," *AIAA Paper 81-1259*, AIAA 14th Fluid and Plasma Dynamics Conference, Palo Alto, CA, USA.
- Mello, O.A.F. and Azevedo, J.L.F., 1998, "Calculation of the Aerodynamic Loads over the VLS Central Body at High Angles of Attack," Report NT-157/ASE-N/98, Instituto de Aeronáutica e Espaço, São José dos Campos, SP, Brazil (in Portuguese).
- Pulliam, T.H. and Steger, J.L., 1980, "Implicit Finite-Difference Simulations of Three-Dimensional Compressible Flow," *AIAA Journal*, Vol. 18, No. 2, pp. 159-167.
- Turkel, E. and Vatsa, V.N., 1994, "Effect of Artificial Viscosity on Three-Dimensional Flow Solutions," *AIAA Journal*, Vol. 32, No. 1, pp. 39-45.